Research Article | Vol. 27, No. 22 / 28 October 2019 / Optics Express 32193

Optics EXPRESS

Two-dimensional photoelectron holography in strong-field tunneling ionization by counter rotating two-color circularly polarized laser pulses

QINGHUA KE,[1] YUEMING ZHOU,[1,4] JIA TAN,[1] MINGRUI HE,[1] JINTAI LIANG,[1] YONG ZHAO,[1] MIN LI,[1] AND PEIXIANG LU[1,2,3]

[1]School of Physics and Wuhan National Laboratory for Optoelectronics, Huazhong University of Science and Technology, Wuhan 430074, China
[2]Hubei Key Laboratory of Optical Information and Pattern Recognition, Wuhan Institute of Technology, Wuhan 430205, China
[3]lupeixiang@hust.edu.cn
[4]zhouymhust@hust.edu.cn

Abstract: Strong-field photoelectron holography (SFPH), originating from the interference of the direct electron and the rescattering electron in tunneling ionization, is a significant tool for probing structure and electronic dynamics in molecules. We theoretically study SFPH by counter rotating two-color circularly (CRTC) polarized laser pulses. Different from the case of the linearly polarized laser field, where the holographic structure in the photoelectron momentum distribution (PEMD) is clustered around the laser polarization direction, in the CRTC laser fields, the tunneling ionized electrons could recollide with the parent ion from different angles and thus the photoelectron hologram appears in the whole plane of laser polarization. This property enables structural information delivered by the electrons scattering the molecule from different angles to be recorded in the two-dimensional photoelectron hologram. Moreover, the electrons tunneling at different laser cycles are streaked to different angles in the two-dimensional polarization plane. This property enables us to probe the sub-cycle electronic dynamics in molecules over a long time window with the multiple-cycle CRTC laser pulses.

1. Introduction

Tunneling ionization is a fundamental process in the laser-matter interaction. When the atom or molecule is exposed to the strong laser fields, the electrons can tunnel through the potential barrier formed by the Coulomb potential and the laser fields [1]. A fraction of the tunneling electrons could be driven back to the parent ion by the laser field and then scatter off or recombine with the ion [2], which gives rise to many interesting phenomena, including high-order above threshold ionization [3–5], nonsequential double ionization [6–12] and high-order harmonic generation [13–17]. During the past decades, these processes have attracted increasing interest in strong field physics and their applications have been widely explored in attosecond science, such as laser-induced electron diffraction [18–21], attosecond pulse generation [22–25] and molecular orbital tomography [26], etc.

Due to the coherent nature of the tunneling electron wave packet (EWP), the direct electron, which reaches the detector without interaction with the parent ion after tunneling ionization, and can interfere with the near-forward rescattering electron, which scatters off the ion before reaching the detector, in the momentum space, known as photoelectron holography [27]. The photoelectron hologram has been firstly observed in strong field tunneling ionization of excited metastable Xenon using a 7 μm free-electron laser pulse [27]. The criteria for observation of this hologram has also been investigated [28]. It has been revealed that the holographic pattern is

#376210 https://doi.org/10.1364/OE.27.032193
Journal © 2019 Received 27 Aug 2019; revised 8 Oct 2019; accepted 8 Oct 2019; published 21 Oct 2019

Optics EXPRESS

more favorably observed at long wavelength and high laser intensity [28,29]. Subsequently, this holographic pattern in the photoelectron momentum distribution (PEMD) has been observed in other atoms and molecules with a wide range of laser parameters [30–34]. In the following years, strong-field photoelectron holography (SFPH) has attracted intensive attention [35–37], and it is suggested to be an important method for probing structure [38] and electronic dynamics in molecules [33,39,40].

Numerically solving the time-dependent Schrödinger equation (TDSE) can well reproduce the holographic patterns in the PEMDs of experiments [27], while the physical process for the holographic structure is not transparent. Instead, strong field approximation (SFA) could provide an intuitive physical picture, and it is demonstrated that the holographic interference pattern can be qualitatively understood by analyzing the phase difference between the direct electron and the rescattering electron [27]. However, the phase difference given by SFA fails in quantitatively describing the holographic patterns [29], which hinders the applications of SFPH. Recently, with adiabatic theory [41], we obtain the phase difference at the quantitative level [38]. The phase difference contains the phase of scattering amplitude, which is a fundamental physical quantity characterizing the structure of the atoms and molecules. In our work [38], a method of retrieving this quantity from the holographic interference structure in the PEMDs has been demonstrated.

SFPH could also provide insight into tunneling process itself [30,31,42–48]. For example, by analyzing the cutoff energy of low-energy holographic structure in the PEMDs, the distance between the electron and the ion at the moment of tunneling ionization was experimentally determined [42]. For tunneling ionization of molecules, the initial phase of the continuum wave packets can also be extracted [30,31]. Lately, we have demonstrated that by adding an orthogonally polarized perturbative laser field and analyzing the response of the holographic interference pattern to the perturbation, the ionization time [43,44] and the initial longitudinal momentum [45] can be retrieved.

Moreover, SFPH is a significant tool for probing electronic dynamics in the atoms and molecules [33,39]. The imprint of coupled electronic and nuclear dynamics on the holographic interference pattern has been observed [33]. Very recently, we have developed an approach to directly visualize the motion of valence electron based on SFPH, wherein the charge migration in molecules has been probed with attosecond temporal resolution [39]. In the multiple-cycle linearly polarized laser pulses, the electrons releasing within different laser cycles overlap in the PEMDs, which smears out the electronic dynamics encoded in the holographic interference structure. Thus, the few-cycle laser pulse is necessary for probing the ultrafast electronic dynamics with SFPH in previous works. Moreover, most of the previous studies on SFPH are focused on the linearly polarized laser fields, where the holographic interference structure in the PEMDs is clustered around the laser polarization direction, and limited information is recorded in the PEMDs.

In this work, we show that with the multiple-cycle counter rotating two-color circularly (CRTC) polarized laser fields [49–52], the photoelectron hologram appears in the whole two-dimensional PEMDs, and thus more structural and dynamical information is encoded therein. In the CRTC laser fields, the electrons ionized during different laser cycles are mapped to different angles in the PEMDs [52]. The electronic dynamics during different laser cycles is recorded in the holographic interference pattern at different angles and the sub-cycle electronic dynamics within one laser cycle is stored along the radial direction in the PEMDs. Here, the angular and radial directions could serve as the coarse and fine pointers of a clock, respectively. By analyzing the holographic interference pattern at different angles in the PEMDs, the sub-cycle electronic dynamics in different laser cycles could be obtained. This property enables one to probe electronic dynamics over a time window as long as several laser cycles with sub-cycle temporal resolution.

In strong field tunneling ionization by the linearly polarized laser pulse, there are many different types of interference patterns in the PEMDs [35,53] and they overlap with each other, making it

Optics EXPRESS

difficult to extract structural and dynamical information from the PEMDs. In the CRTC fields, different interference patterns can be selectively enhanced or suppressed, and separated in the PEMDs, facilitating structural and dynamical information retrieval. Moreover, the distributions of the holographic pattern at different angles correspond to the electrons recolliding the parent ion from different angles. We demonstrate that this property enables one to probe molecular structure by the electrons rescattering from different angles. We should mention that the two-color circularly polarized laser fields have been widely used to control the electronic dynamics in strong field ionization [54–68] and high-order harmonic generation [69–72]. In this paper, we mainly focus on the holographic interference structure in the PEMDs by the CRTC laser fields.

The main body of this paper is organized as follows. In section 2, we introduce the theoretical method in our calculations, i.e., numerically solving the TDSE. Section 3 consists of three subsections. First, we present how to manipulate holographic interference structures. Then, we demonstrate that the holographic fringe contains two-dimensional structure information and dynamical information of valence electron in molecules. Section 4 is a brief conclusion. Throughout this paper, atomic units (a.u.) are used unless otherwise noted.

2. Numerically solving the TDSE

In this paper, PEMDs are obtained by numerically solving the two-dimensional TDSE. With the single active electron approximation, the TDSE is

$$i\frac{\partial\psi(\mathbf{r},t)}{\partial t} = H(\mathbf{r},t)\psi(\mathbf{r},t), \tag{1}$$

where the Hamiltonian in length gauge is

$$H(\mathbf{r},t) = -\frac{1}{2}\nabla^2 + V(x,y) + \mathbf{r}\cdot\mathbf{E}(t). \tag{2}$$

$\mathbf{r} = (x,y)$ is the coordinate of the electron, and $\mathbf{E}(t)$ is the electric field. $V(x,y)$ is the interaction potential between the electron and the ion. In this paper, we study both atomic and molecular targets. For the atom,

$$V(x,y) = -\frac{1}{\sqrt{x^2+y^2+a}}, \tag{3}$$

where a set to 0.39 to match the ground state energy (−0.579 a.u.) of argon atom. For the molecule,

$$V(x,y) = -\frac{1}{\sqrt{(x+R/2)^2+y^2+a}} - \frac{1}{\sqrt{(x-R/2)^2+y^2+a}}, \tag{4}$$

which mimics the potential of H_2^+ molecule with the internuclear distance $R = 4$ a.u. The two nuclei are fixed at $(-R/2,0)$ and $(R/2,0)$. a is set to 0.715, and the eigenenergies of the ground state ($1s\sigma_g$) and the first excited state ($2p\sigma_u$) are $E_0 = -0.796$ a.u. and $E_1 = -0.655$ a.u., respectively. The counter rotating two-color circularly polarized field consists of the left circularly polarized field

$$\mathbf{E}_l = f(t)E_1[\mathbf{x}\cos(\omega_1 t+\varphi_1) + \mathbf{y}\sin(\omega_1 t+\varphi_1)], \tag{5}$$

and the right circularly polarized field

$$\mathbf{E}_r = f(t)E_2[\mathbf{x}\cos(\omega_2 t+\varphi_2) - \mathbf{y}\sin(\omega_2 t+\varphi_2)]. \tag{6}$$

The total electric field is

$$\begin{aligned}\mathbf{E}(t) = \mathbf{E}_l + \mathbf{E}_r = {} & f(t)\mathbf{x}[E_1\cos(\omega_1 t+\varphi_1) + E_2\cos(\omega_2 t+\varphi_2)] \\ & + f(t)\mathbf{y}[E_1\sin(\omega_1 t+\varphi_1) - E_2\sin(\omega_2 t+\varphi_2)].\end{aligned} \tag{7}$$

Here, ω_1 (ω_2) is the angular frequency of the left (right) circularly polarized fields with the wavelength $\lambda_1 = 800$ nm ($\lambda_2 = 1200$ nm), and thus the total electric field exhibits a 5-fold

Optics EXPRESS

rotation symmetry [64]. The total electric field has the trapezoid envelope form $f(t)$ that rises and falls in $3T_1$ ($T_1 = 2\pi/\omega_1$), with a platform of $4T_1$. E_1 (E_2) is the amplitude of the left (right) circularly polarized fields. The intensity of the left circularly polarized laser field I_1 is fixed at 1.0×10^{14} W/cm^2, and the intensity of the right circularly polarized laser field is given by the relation $I_2 = I_1 \cdot \mathscr{R}$, where $\mathscr{R}$ denotes the intensity ratio of two circular fields. φ_1 is always set to 0 without loss of generality, and the relative phase of two circularly polarized fields reads $\Delta\varphi = \varphi_2 - \varphi_1 = \varphi_2$.

The split-operator spectral method is used to numerically solve the two-dimensional TDSE in Cartesian coordinate [73]. To eliminate the nonphysical effect of the reflection of EWPs at the grid space boundary, we divide the whole grid space into two regions, inner region $(0 - R_c)$ and outer region $(R_c - R_{max})$, where R_c is the absorbing boundary and R_{max} is the boundary of the whole grid space [74]. The wavefunction of the electron at time τ is

$$\Psi(\tau) = \Psi(\tau)[1 - F_s(R_c)] + \Psi(\tau)F_s(R_c) = \Psi_{in}(\tau) + \Psi_{out}(\tau). \tag{8}$$

Here, $F_s(R_c) = 1/(1 + \exp(-(\sqrt{x^2 + y^2} - R_c)/\Delta))$ is the absorbing function, and Δ is the width of the crossover region. Ψ_{in} follows the Schrödinger equation with total Hamiltonian (Eq. (2)), and Ψ_{out} propagates under Volkov Hamiltonian (without the Coulomb potential term) [75,76]. At the end of each time step, the wavefunction of outer region $\Psi_{out}(\tau)$ is Fourier transformed into the momentum space $C(\mathbf{p}, \tau)$. Then, $C(\mathbf{p}, \tau)$ propagates under Volkov Hamiltonian from time τ to the end of the laser pulse, with $\overline{C}(\mathbf{p}, \tau) = \exp\{-i \int_\tau^\infty \frac{1}{2}[\mathbf{p} + \mathbf{A}(\tau')]^2 d\tau'\} C(\mathbf{p}, \tau)$, where $\mathbf{A}(\tau') = -\int_0^{\tau'} \mathbf{E}(t')dt'$ is the vector potential of the laser field. The final photoelectron momentum distribution is obtained by adding up all the wavefunctions in the momentum space for each time step, and it has the form

$$\frac{dP(\mathbf{p})}{dEd\theta} = |\sum_\tau \overline{C}(\mathbf{p}, \tau)|^2, \tag{9}$$

where E is the final energy of the electron with $E = \mathbf{p}^2/2$ and θ is its emission angle. The initial wavefunction is obtained by the imaginary time propagation method [77,78].

In our numerical simulations, the time step of propagation is $\Delta t = 0.1$ a.u. The Cartesian grid space ranges from -400 a.u. to 400 a.u. for both x-axis and y-axis directions with a grid size of $\Delta x = \Delta y = 0.2$ a.u. The inner space boundary is $R_c = 100$ a.u. with $\Delta = 4$ a.u.

3. Results and discussions

3.1. Interference structures in the PEMDs

Figure 1(a) shows the PEMD of Ar ionized by the linear laser pulse polarized along y-axis. The wavelength and peak intensity of this laser pulse are 1200 nm and 1.5×10^{14} W/cm^2, respectively. Figure 1(b) displays the PEMD obtained by the CRTC laser pulse (Eq. (7)). The intensities of left (800 nm) and right (1200 nm) circularly polarized laser pulses are 1.0×10^{14} W/cm^2 and 5×10^{13} W/cm^2, respectively. For the linearly polarized laser field, the photoelectrons mainly distribute along the polarization direction, as shown in Fig. 1(a). Different types of interference patterns are visible in the PEMDs. The ring-like structure most visible in the low-energy region is the well-known above threshold ionization (ATI) peaks [3]. The fork-like interference along p_y axis is the holographic structure, which has been widely studied in previous works [27,38,39,43]. For the CRTC fields, the electrons distribute in the whole two-dimensional polarization plane, as shown in Fig. 1(b), and the interference structures are very different from those in Fig. 1(a) using the linearly polarized laser field. To identify different interference patterns in Fig. 1(b), we focus on the branch in the first quadrant of the PEMDs indicated by the white box as an example. The electric field and the corresponding negative vector potential of the CRTC laser pulse are plotted in Figs. 2(a) and 2(b), respectively. The electric field and the negative vector potential in two successive quarter-cycles Q1 and Q2 are highlighted by blue and red colors, respectively.

Optics EXPRESS

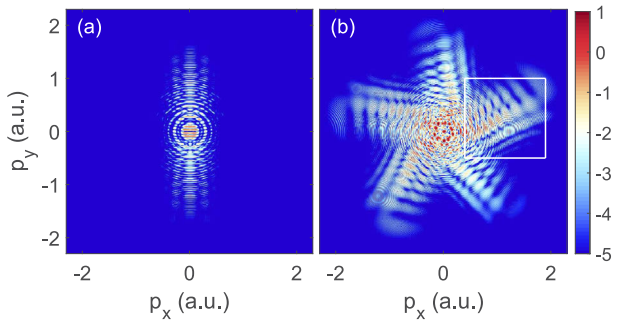

Fig. 1. The PEMDs in logarithmic scale of Ar ionized by (a) the linear laser pulse polarized along y-axis, and (b) the CRTC laser pulse. The wavelength and intensity of the linearly polarized laser pulse are 1200 nm and 1.5×10^{14} W/cm^2, respectively. For the CRTC laser pulse, the intensities of left (800 nm) and right (1200 nm) circularly polarized laser pulses are 1.0×10^{14} W/cm^2 and 5×10^{13} W/cm^2, respectively. The relative phase of the CRTC laser pulse is $\Delta\varphi = 0$. Both the linearly polarized laser pulse and the CRTC laser pulse have the total duration time of 10 T_1 with the trapezoid envelope $f(t)$.

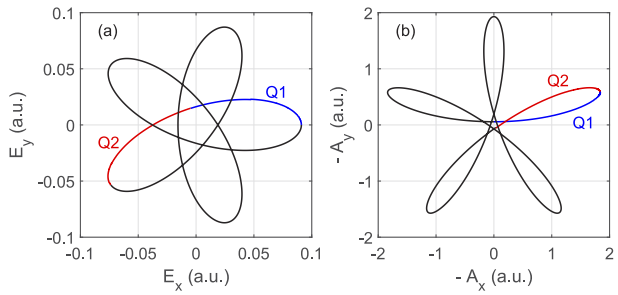

Fig. 2. The CRTC laser field (a) and the corresponding negative vector potential (b) used in Fig. 1(b). The labels Q1 and Q2 represent two successive quarter-cycles of the CRTC laser pulse.

Figure 3(a) shows the enlarged view of the PEMD in the white box in Fig. 1(b). Three types of interference patterns are visible, as marked by (i), (ii) and (iii), wherein the maxima of the interference patterns are shown by the yellow dashed, magenta dot-dashed and black solid lines, respectively. According to Fig. 2(b), it's known that the electrons distributed in the first quadrant are ionized during the two successive quarters of the laser cycle Q1 and Q2. Note that the electrons ionized during Q1 could return back to the parent ion. Thus, there are two types of orbits within Q1, i.e. the direct electron and rescattering electron. The electrons ionized during Q2 cannot return back to the parent ion and thus only the direct electron exists. The origination of the different types of the interference structures in the PEMD could be identified by analyzing the phases of these orbits within the strong-field approximation (SFA) [27] or semiclassical model [63].

With SFA, the phase of the direct electrons ionized during Q1 or Q2 reads

$$S_d = \frac{1}{2}\int_{t_0^{di}}^{t} d\tau[\mathbf{p} + \mathbf{A}(\tau)]^2 - I_p t_0^{di}, \tag{10}$$

where t_0^{di} $(i = 1, 2)$ denotes the direct electrons ionized during Q1 or Q2, $\mathbf{p}$ is the asymptotic momentum of the direct electron and I_p is the ionization energy. The phase of the scattering

Optics EXPRESS

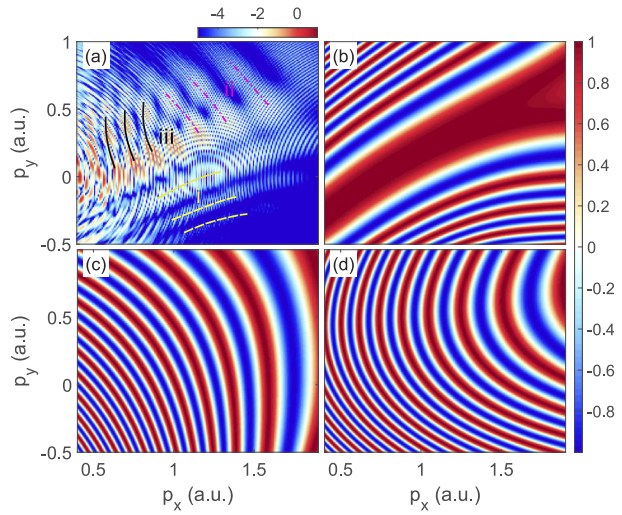

Fig. 3. (a) The enlarged view of the PEMD in the white box of Fig. 1(b). Three interference patterns in the PEMD are marked as (i), (ii) and (iii). The yellow dashed, magenta dot-dashed and black solid lines show the maxima of the interference patterns (i), (ii) and (iii), respectively. (b) is the interference pattern between the direct electrons and the rescattering electrons ionized during Q1. (c) is the interference pattern between the direct electrons ionized during Q1 and the rescattering electron ionized within Q2. (d) is the interference pattern between direct electrons ionized during Q1 and Q2.

electron ionized during Q1 is

$$S_r = \frac{1}{2}\int_{t_r}^{t} d\tau[\mathbf{p} + \mathbf{A}(\tau)]^2 + \frac{1}{2}\int_{t_0^r}^{t_r} d\tau[\mathbf{k} + \mathbf{A}(\tau)]^2 - I_p t_0^r. \tag{11}$$

Here, t_0^r, t_r and $\mathbf{k}$ are the ionization time, the rescattering time and intermediate momentum of the rescattering electron. These can be calculated by solving the saddle-point equations [5,27].

The phase difference between the direct electron ionized during Q1 or Q2 and the rescattering electron ionized during Q1 reads

$$\Delta S = S_d - S_r = \frac{1}{2}\int_{t_0^{di}}^{t_r} d\tau[\mathbf{p} + \mathbf{A}(\tau)]^2 - \frac{1}{2}\int_{t_0^r}^{t_r} d\tau[\mathbf{k} + \mathbf{A}(\tau)]^2 + I_p(t_0^r - t_0^{di}). \tag{12}$$

Similarly, the phase difference between direct electrons ionized during Q2 and Q1 is

$$\Delta S = S_{d2} - S_{d1} = \frac{1}{2}\int_{t_0^{d1}}^{t_0^{d2}} d\tau[\mathbf{p} + \mathbf{A}(\tau)]^2 + I_p(t_0^{d1} - t_0^{d2}). \tag{13}$$

The interference structures between the direct electrons ionized within Q1 and Q2 and the rescattering electron ionized during Q1, calculated with Eq. (12), are shown in Figs. 3(b) and 3(c), respectively. Figure 3(d) shows the interference pattern for the direct electrons ionized during Q1 and Q2 calculated with Eq. (13). Comparison of these results with Fig. 3(a), the origination of the interference patterns (i), (ii) and (iii) in Fig. 3(a) could be determined. The interference (i) in the radial direction corresponds to the interference between the direct electron and the scattering electron ionized within the same quarter-cycle Q1, i.e. the holographic interference, as shown in Fig. 3(b). The interferences (ii) and (iii) exhibit the similar interference structures and fringe spacing as Fig. 3(c) and Fig. 3(d), respectively.

Optics EXPRESS

Figure 3(a) shows that three types of interference patterns dominate at different areas in the PEMDs. This can be directly understood by analyzing the negative vector potential of the CRTC laser pulse in Fig. 2(b). According to Fig. 2(b), the direct electrons ionized in Q1 and Q2 reach the right-lower and left-upper regions in Fig. 3(a), respectively. Thus, the holographic interference pattern (i), which results from the forward rescattering electron and the direct electron ionized during Q1, is dominant at the right-lower region in Fig. 3(a). Whereas the interference pattern (ii), originating from the forward rescattering electron ionized within Q1 and the direct electron ionized during Q2, emerges at the left-upper area in Fig. 3(a). For the area near the momentum origin, the vector potentials of Q1 and Q2 are close to each other, and thus the direct electrons ionized during Q1 and Q2 could interfere, giving rise to the interference pattern (iii) in Fig. 3(a). In this CRTC field, these different interference structures are separated from each other in the PEMDs. We should mention that in the linearly polarized laser pulses these interference patterns overlap in the PEMDs.

In our previous work [63], we have identified different interference patterns in the bicircular two-color laser fields by the semiclassical rescattering model. In this paper, the origination of these interference patterns, as well as their positions, are straightforwardly explained by the vector potential of the laser fields. In addition, we will reveal how to selectively enhanced or suppressed the specific interference structures. More importantly, we demonstrate how the structural and dynamical information of the target are encoded in the two-dimensional holographic interferences, and the possibility of extracting these information.

By changing the intensity ratio, the interference structures could be selectively enhanced or suppressed. Figure 4 shows the PEMDs with different intensity ratios with the relative phase $\Delta\varphi = 0$. When the intensity ratio is close to 1 (Figs. 4(a) and 4(b)), the interference pattern (iii) between direct electrons ionized within Q1 and Q2 (not labeled here) dominates in the PEMDs since the vector potentials within Q1 and Q2 are close to each other in a wide range of momentum region. When the intensity ratio is 0.5, the electron ionized during Q1 is most likely to return back and scatter with the ion [59]. Thus, the interference patterns (i and ii) between the direct and rescattering electron are most visible, as shown in Fig. 4(c), while the interference pattern (iii) between the direct electrons only appears near the momentum origin, as explained above. As the intensity ratio further decreases, the vector potentials of Q1 and Q2 become more separated and thus the interference pattern (iii) is strongly suppressed, and only the interference pattern (ii) is visible in the PEMD.

Due to the rescattering process, the photoelectron holography could be employed to probe the structural information of parent ion. To probe molecular target, it is necessary to recollide with the target from different angles. In the CRTC laser field, the electrons ionized within different laser cycles recollide with the parent ion from different angles and finally locate at different areas in the PEMDs. Thus, the two-dimensional holographic interference patterns could encode much more structural information of the target than the linear case. Moreover, the incident angle of the returning electron can be controlled by changing the relative phase of the two fields, enabling one to probe molecules from different angles. As an example, Fig. 5 shows the PEMDs of argon atom (top panels) and H_2^+ molecule (bottom panels) ionized by the CRTC laser pulse with different relative phases. Comparing with the PEMDs of relative phase 0 (left panels), the PEMDs of relative phase 0.5π (right panels) rotate clockwise by 54°.

3.2. Structural information recorded by the 2D hologram in the PEMDs

In this paper, we will focus on the holographic interference between the direct and rescattering electrons ionized during the same quarter of the laser field. For this type of interference, the ionization times in Eq. (12) for the direct and rescattering electrons are approximately the same,

Optics EXPRESS

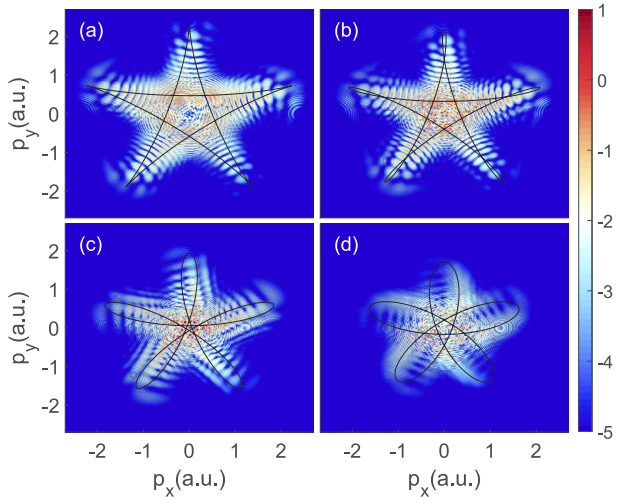

Fig. 4. The PEMDs in logarithmic scale of Ar ionized by the CRTC laser pulses with the intensity ratios $\mathscr{R}$ of (a) 1, (b) 0.8, (c) 0.5 and (d) 0.3. The intensity of left (800 nm) circularly polarized laser pulse I_1 is fixed at 1.0×10^{14} W/cm^2, and the intensity of right (1200 nm) circularly polarized laser pulse is given by $I_2 = I_1 \cdot \mathscr{R}$. The corresponding negative vector potentials are plotted in the PEMDs with black solid curves. The relative phase of two circular fields is fixed at $\Delta\varphi = 0$.

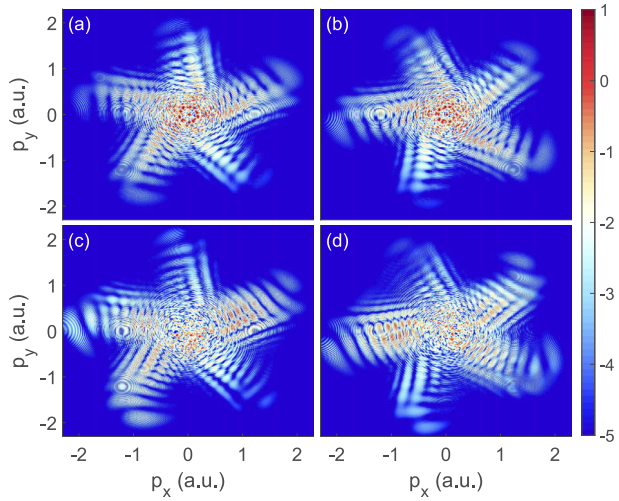

Fig. 5. The PEMDs in logarithmic scale of Ar (top panels) and H_2^+ (bottom panels) ionized by the CRTC pulses with the relative phase of 0 (left panels) and 0.5π (right panels). Other laser parameters are the same as Fig. 4(c).

i.e. $t_0^r \approx t_0^{d1} = t_0$, and thus the phase difference given by Eq. (12) could be written as

$$\Delta S \approx \frac{1}{2}\int_{t_0}^{t_r} d\tau\{[\mathbf{p} + \mathbf{A}(\tau)]^2 - [\mathbf{k} + \mathbf{A}(\tau)]^2\}. \tag{14}$$

Note that for the linear laser pulse, the phase difference reads $\Delta S \approx p_\perp^2(t_r - t_0)/2$ as given in previous literatures [27–29], where $p_\perp$ is the final momentum perpendicular to the laser

Optics EXPRESS

polarization direction. In the formula (14), the phase difference for the holographic interference structure is determined by the laser field and no target information is encoded. This formula could produce the overall shape of the interference structure. However, it fails at the quantitative level.

With the adiabatic theory [41], we have derived a more accurate description for the phase difference [38]. In this paper, for the static state, the phase difference between the direct electron and rescattering electron reads

$$\Delta\Phi = \Delta S + \alpha. \tag{15}$$

The first term is the same as Eq. (12). It accounts for the phase difference between the direct electron and the rescattering electron during their propagation in the CRTC laser fields. The second term $\alpha = \alpha(p, \phi)$ is the phase of the scattering amplitude and it characterizes the atomic and molecular structure. It indicates that the holographic patterns encode structure information of the targets, and thus the holographic interference fringes in the PEMDs should be different for Ar (upper panels) and H_2^+ (bottom panels) in Fig. 5.

To demonstrate this difference of the holographic interference fringes, we transform the PEMDs in Figs. 5(b) and 5(d) into the polar coordinate, as shown in Figs. 6(a) and 6(b). The low-energy part ($p_r = \sqrt{p_x^2 + p_y^2}$<0.5 a.u.) is not shown in the PEMDs because the interference structures are not visible. Note that we have normalized the PEMDs for each polar angle θ. The nearly vertical interference pattern in Fig. 6 is the holographic interference pattern (i), and the horizontal interference patterns correspond to the other two interference structures (ii and iii).

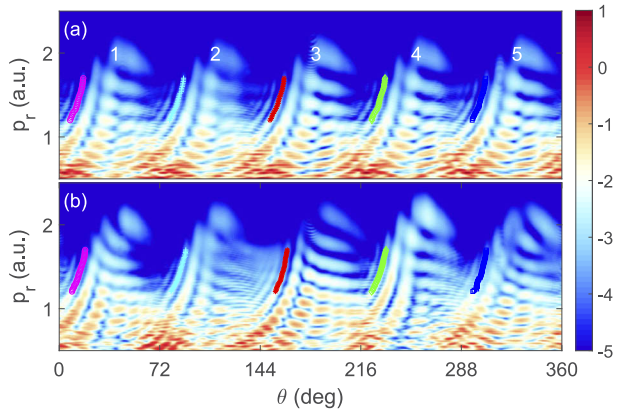

Fig. 6. The PEMDs (arbitrary units in logarithmic scale) in the polar coordinate of (a) Ar and (b) H_2^+ of ground state. The PEMD intensity is in logarithmic scale. The maxima of holographic interference fringes are marked with different symbols. The five branches of the PEMDs in the polar coordinate are labeled by the numbers.

Moreover, Figs. 7(a) and 7(b) display the slices of the PEMDs for Ar and H_2^+ at $p_r = 1.4$ a.u. as a function of polar angle θ. The five branches of the PEMDs in the polar coordinate are labeled by 1 (0°<θ<72°), 2 (72°<θ<144°), 3 (144°<θ<216°), 4 (216°<θ<288°) and 5 (288°<θ<360°) from left to right in Fig. 6(a). Due to the 5-fold symmetry of the electric field (see Fig. 2), the slices can be shifted to the same angular range for comparison. Figures 7(a) and 7(b) are the results for Ar and H_2^+, respectively. The slices are shifted to the same angular range for comparison. For Ar, the curves for five branches coincide. While for H_2^+, there is an obvious shift among these curves. Moreover, to describe the holographic interference patterns, we trace the maxima of holographic interference fringes for the five branches (indicated by the symbols in Fig. 6) with p_r ranging from 1.2 a.u. to 1.7 a.u. Figures 7(c) and 7(d) show the extracted maxima

Optics EXPRESS

shifted to the same angular range from Figs. 6(a) and 6(b) for comparison. We can clearly see the difference between the extracted fringes from the PEMDs of Ar (Fig. 7(c)) and H_2^+ (Fig. 7(d)). In Fig. 7(c), the fringes for five branches coincide, while in Fig. 7(d), there is a shift among fringes.

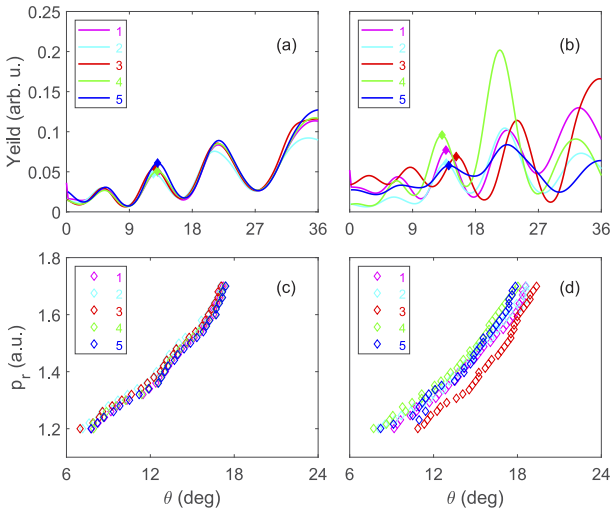

Fig. 7. The slices from the PEMDs of (a) Ar and (b) H_2^+ at $p_r = 1.4$ a.u. as a function of polar angle. These curves are shifted to the same angular range. The holographic interference maxima at $p_r = 1.4$ a.u. are also indicated by the solid diamonds in (a) and (b). The maxima in Figs. 6(a) and 6(b) with p_r ranging from 1.2 a.u. to 1.7 a.u. are shifted to the same angular range, shown in (c) and (d).

The shift among the holographic fringes can be understood as following. For the static state, the holographic interference pattern is determined by the phase difference Eq. (15). The first term accounts for the phase difference between the direct electron and the rescattering electron during their propagation in the laser fields. It is the same for the five branches in the PEMDs for both Ar and H_2^+. The shift is attributed to the second term α. For Ar, the phase α for the electron rescattering the ion with different incident angles is the same due to the 5-fold symmetry of the laser fields. Thus, the second term α in Eq. (15) is the same for the five branches and the PEMD of argon exhibits a 5-fold rotation symmetry. For H_2^+, the phase α depends on the incident angle. Thus, the second term α in Eq. (15) is different for the five branches in the PEMD. Consequently, it accounts for the visible phase shift in the holographic fringes for the five branches, as shown in Figs. 7(b) and 7(d). These results indicate that the structure of the targets could be probed by the electrons scattering from different angles, and the delivered information is indeed recorded in the holographic pattern. By changing the relative phase of the CRTC fields (see Fig. 5), the incident angles of the rescattering electrons can be continuously manipulated. Thus, the targets could be probed from different angles and the structural information could be recorded in the two-dimensional photoelectron hologram.

3.3. *Electronic dynamics recorded by the 2D hologram in the PEMDs*

Holographic interference pattern also records dynamical process of the valence electron in atoms and molecules. As an example, we show the electronic dynamics for the electron in the superposition state in H_2^+,

$$\psi(\mathbf{r}, t) = c_0\psi_0(\mathbf{r})e^{-iE_0t} + c_1\psi_1(\mathbf{r})e^{-iE_1t}, \tag{16}$$

Optics EXPRESS

where $\psi_0(\mathbf{r})$ and $\psi_1(\mathbf{r})$ are the wavefunctions of ground state ($1s\sigma_g$) and first excited state ($2p\sigma_u$), separately. E_0 and E_1, c_0 and c_1 are corresponding eigenenergies and expansion coefficients, respectively. For this superposition state, the electron wave packet oscillates between two fixed nuclei with a period of $2\pi/(E_1 - E_0)$. Figure 8(a) shows the PEMD of this superposition state ionized by a linearly polarized laser pulse, wherein the polarization direction is perpendicular to the molecular axis and the laser pulse has a duration of $3T_2$ ($T_2 = 2\pi/\omega_2$) with $\sin^2$ envelope. It is shown that the positions of the holographic interference minima and maxima in the PEMD are obviously asymmetric about p_y axis. In our previous work [39], we have demonstrated that this asymmetry and its dependence on p_y record the coherent electronic dynamics of the superposition state with attosecond temporal resolution. However, when a 7-cycle linearly polarized laser pulse with the trapezoid envelope that rises and falls in $2T_2$ is applied, as shown in Fig. 8(b), the PEMD becomes symmetric with respect to p_y axis. Moreover, the holographic interference structure becomes more obscured in Fig. 8(b). The reason is that in the multiple-cycle linearly polarized laser field, the electrons ionized during different cycles overlap in the PEMDs. Hence, the dynamical information recorded by the hologram is averaged out in Fig. 8(b).

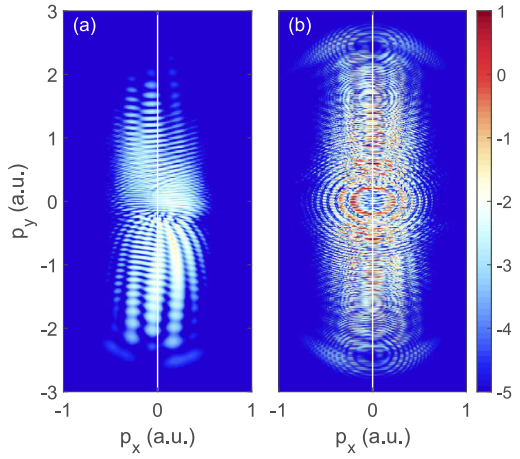

Fig. 8. The PEMDs in logarithmic scale of the superposition state ionized by the few-cycle (a) and the multiple-cycle (b) linearly polarized pulses. The wavelength and peak intensity of the laser pulses are 1200 nm and 3.0×10^{14} W/cm^2, respectively. The expansion coefficients c_0 and c_1 for the superposition state (Eq. (16)) are set to $1/\sqrt{5}$ and $2/\sqrt{5}$.

In the CRTC laser fields, the electrons ionized within different laser cycles are mapped to different angles and thus the clear interference patterns are still visible in the PEMDs. Consequently, the sub-cycle electronic dynamics could be recorded by the photoelectron hologram even with the multiple-cycle CRTC laser pulses. To show this property, we expose H_2^+ to the CRTC laser fields. Figure 9(b) is the PEMD in polar coordinate for tunneling ionization of the electron in the superposition state by the CRTC field with a duration of $10T_1$, where $T_1 = 2\pi/\omega_1$, and Fig. 9(a) shows the PEMD of the ground state ($1s\sigma_g$) for comparison. For the superposition state, the phase difference $\Delta\Phi$ between the direct electron and the rescattering electron has three contributions [38,39,41]

$$\Delta\Phi = \Delta S + \alpha + \delta\phi. \tag{17}$$

The first two contributions have already been given by Eq. (15). The third term $\delta\phi = \phi_s(0; t_0) - \phi_s(p_\perp; t_0)$ is correlated to the electron motion of the superposition state in the molecule (refer to the supplementary material of Ref. [39]), where $\phi_s(0; t_0)$ and $\phi_s(p_\perp; t_0)$ are the

Optics EXPRESS

initial phase of the rescattering and direct electron at tunneling time t_0, and $p_\perp$ denotes the initial transverse momentum of the direct electron at tunneling time. For the ground state and superposition state, the first two terms at the right side of Eq. (17) are the same for each branch. Thus, the difference in the holographic interference patterns of the same branch in the PEMDs between the superposition state (Fig. 9(b)) and the ground state (Fig. 9(a)) reveals the electronic dynamics induced by the superposition state.

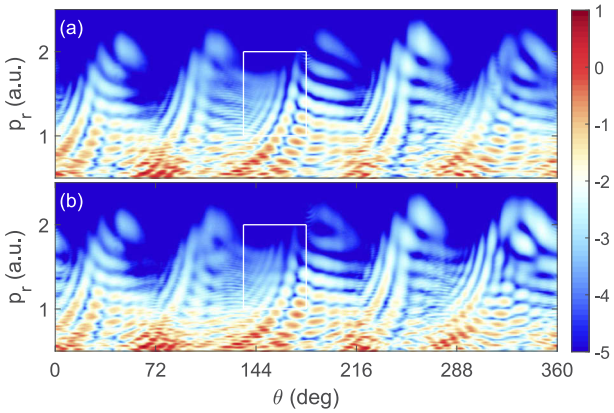

Fig. 9. The PEMDs (arbitrary units in logarithmic scale) in polar coordinate of ground state (a) and superposition state (b) in H_2^+ ionized by the CRTC laser pulses. The PEMD intensity is in logarithmic scale. The laser parameters are the same as those in Fig. 5(b).

To elaborate this difference, we take the third branch ($144°<\theta<216°$) for an example, and the enlarged views of the PEMDs in the white boxes are shown in Figs. 10(a) and 10(b), respectively. The two slices from the PEMDs of ground state and the superposition state are plotted at the middle panel of Fig. 10. Figures 10(c) and 10(d) are results cut at $p_r = 1.6$ a.u. and $p_r = 1.2$ a.u., respectively. The shifts of the holographic interference fringes between the superposition state and ground state at different radial momentum are obvious. To see this feature more clearly, we employ the procedure proposed in Refs. [38,39] to subtract the envelope of the yield curve, and the obtained phase term $\Delta\Phi$ is shown in Figs. 10(e) and 10(f). Obviously, the holographic interference fringes of the superposition state are shifted from those of the ground state, and the shift at $p_r = 1.6$ a.u. is larger than that at $p_r = 1.2$ a.u., which indicates different positions of the electron at different time [39]. Hence, the shift of holographic interference fringes caused by the phase $\delta\phi$ reveals the electron motion induced by the superposition state.

In the CRTC fields, the electrons ionized during different laser cycles distribute at different branches of the PEMDs. The electrons ionized at different time during one laser cycle reach different final radial momentum p_r in one branch of the PEMDs. Thus, the angular direction could serve as the coarse pointer of a clock, and the radial direction serves as the fine pointer which records the sub-cycle dynamics of the electron in molecules. Our results indeed reveal that the sub-cycle electronic dynamics is recorded in the two-dimensional hologram. With the CRTC fields, the electronic dynamics over a time window of several laser cycles could be probed with sub-cycle temporal resolution with the photoelectron holography. The quantitative extraction of the electronic dynamics from this photoelectron hologram is more complicated than the case of the linearly polarized laser field and it is beyond the scope of this paper.

Optics EXPRESS

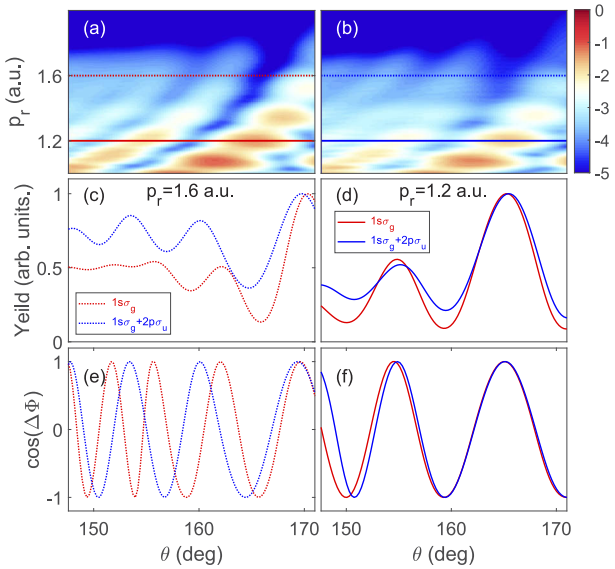

Fig. 10. (a)(b) The PEMDs in the white boxes of Figs. 9(a) and 9(b), respectively. The lines in the PEMDs indicate $p_r = 1.2$ a.u. (solid) and $p_r = 1.6$ a.u. (dotted). Two slices of the PEMDs at $p_r = 1.6$ a.u. and $p_r = 1.2$ a.u. are shown in (c) and (d). The red curve and blue curve are results of ground state and the superposition state. The yields are normalized to the maximum value. (e) and (f) display cos(ΔΦ) extracted from (c) and (d), respectively.

4. Conclusions

We have studied the interference structures in strong field tunneling ionization of the atoms and molecules by the counter rotating two-color circularly polarized fields. Our results show that different types of interference structures in the PEMDs can be separated by the CRTC fields. In particular, by changing the intensity ratio of the CRTC fields, the holographic interference can be selectively enhanced. In the CRTC fields, the electrons ionized within different laser cycles recollide with the parent ion from different angles and finally distribute at different angles in the PEMDs. Thus, the holographic interference structure appears in the whole two-dimensional polarization plane, and it could record more structural information of the targets than the case of linearly polarized laser pulses. As an example, we reveal the clear shift of the interference fringes for different branches in the PEMDs of H_2^+ molecule. This shift is due to the fact that the phase of elastic scattering amplitude for molecules depends on the incident angle of the returning electron. In the CRTC fields, the molecule could be probed by the electrons scattering from different angles in single-shot measurements. Moreover, in the CRTC fields, the electrons ionized during different laser cycles finally locate at different angles in the PEMDs, which enables us to probe the electronic dynamics in molecules even with the multiple-cycle laser pulses. We show that the hint about the ultrafast electronic dynamics induced by the superposition state survives in the multiple-cycle CRTC laser pulses, while it is averaged out in the linearly polarized laser pulses.

Our results show that the CRTC field involved in this paper has at least the following advantages in probing the structural information and ultrafast electronic dynamics in molecules based on SFPH. First, the multiple-cycle pulse is more experimentally feasible compared to the few-cycle laser pulse. Second, the two-dimensional laser pulse results in the holographic interference pattern appearing in the whole laser polarization plane and thus richer structural information of molecules is encoded in the PEMDs. Third, the CRTC laser pulse provides a time window of several laser cycles for recording the electronic dynamics with sub-cycle temporal resolution.

Optics EXPRESS

These properties indicate that the CRTC field could be a very promising tool in probing the structure and electronic dynamics in molecules with the concept of strong-field photoelectron holography. In this paper, we revealed target information and electronic dynamics at qualitative level, quantitative information could be extracted in more complex systems within our scheme in the future work.

Funding

National Natural Science Foundation of China (11604108, 11622431, 11627809, 11874163).

Acknowledgments

Numerical simulations presented in this paper were carried out using the High Performance Computing Center experimental testbed in SCTS/CGCL (see http://grid.hust.edu.cn/hpcc).

References

1. L. V. Keldysh, "Ionization in the Field of a Strong Electromagnetic Wave," Sov. Phys. JETP **20**, 1307 (1965).
2. P. B. Corkum, "Plasma perspective on strong field multiphoton ionization," Phys. Rev. Lett. **71**(13), 1994–1997 (1993).
3. P. Agostini, F. Fabre, G. Mainfray, G. Petite, and N. K. Rahman, "Free-Free Transitions Following Six-Photon Ionization of Xenon Atoms," Phys. Rev. Lett. **42**(17), 1127–1130 (1979).
4. G. G. Paulus, W. Nicklich, Huale Xu, P. Lambropoulos, and H. Walther, "Plateau in above threshold ionization spectra," Phys. Rev. Lett. **72**(18), 2851–2854 (1994).
5. W. Becker, F. Grasbon, R. Kopold, D. B. Milosevic, G. G. Paulus, and H. Walther, "Above-threshold ionization: From classical features to quantum effect," Adv. At., Mol., Opt. Phys. **48**, 35–98 (2002).
6. W. Becker, X. Liu, P. J. Ho, and J. H. Eberly, "Theories of photoelectron correlation in laser-driven multiple atomic ionization," Rev. Mod. Phys. **84**(3), 1011–1043 (2012).
7. Y. Zhou, Q. Liao, and P. Lu, "Asymmetric electron energy sharing in strong-field double ionization of helium," Phys. Rev. A **82**(5), 053402 (2010).
8. Y. Zhou, C. Huang, and P. Lu, "Coulomb-tail effect of electron-electron interaction on nonsequential double ionization," Phys. Rev. A **84**(2), 023405 (2011).
9. Y. Zhou, C. Huang, A. Tong, Q. Liao, and P. Lu, "Correlated electron dynamics in nonsequential double ionization by orthogonal two-color laser pulses," Opt. Express **19**(3), 2301 (2011).
10. Y. Zhou, C. Huang, Q. Liao, and P. Lu, "Classical Simulations Including Electron Correlations for Sequential Double Ionization," Phys. Rev. Lett. **109**(5), 053004 (2012).
11. Y. Zhao, Y. Zhou, J. Liang, Z. Zeng, Q. Ke, Y. Liu, M. Li, and P. Lu, "Frustrated tunneling ionization in the elliptically polarized strong laser fields," Opt. Express **27**(15), 21689 (2019).
12. A. Tong, Q. Li, X. Ma, Y. Zhou, and P. Lu, "Internal collision induced strong-field nonsequential double ionization in molecules," Opt. Express **27**(5), 6415 (2019).
13. F. Krausz and M. Ivanov, "Attosecond physics," Rev. Mod. Phys. **81**(1), 163–234 (2009).
14. J. Li, Q. Zhang, L. Li, X. Zhu, T. Huang, P. Lan, and P. Lu, "Orientation dependence of high-order harmonic generation in nanowire," Phys. Rev. A **99**(3), 033421 (2019).
15. B. Wang, L. He, Y. Qing, Y. Zhang, R. Shao, P. Lan, and P. Lu, "All-optical measurement of high-order fractional molecular echoes by high-order harmonic generation," Opt. Express **27**(21), 30172 (2019).
16. D. M. Kinyua, L. Niu, H. Long, K. Wang, and B. Wang, "Tuning the photoinduced charge transfer from CdTe quantum dots to ZnO nanofilms through Ga doping," Opt. Mater. **96**, 109311 (2019).
17. D. M. Kinyua, H. Long, X. Xing, S. Njoroge, K. Wang, B. Wang, and P. Lu, "Gigahertz acoustic vibrations of Ga-doped ZnO nanoparticle array," Nanotechnology **30**(30), 305201 (2019).
18. T. Morishita, A.-T. Le, Z. Chen, and C. D. Lin, "Accurate Retrieval of Structural Information from Laser-Induced Photoelectron and High-Order Harmonic Spectra by Few-Cycle Laser Pulses," Phys. Rev. Lett. **100**(1), 013903 (2008).
19. M. Okunishi, T. Morishita, G. Prumper, K. Shimada, C. D. Lin, S. Watanabe, and K. Ueda, "Experimental Retrieval of Target Structure Information from Laser-Induced Rescattered Photoelectron Momentum Distributions," Phys. Rev. Lett. **100**(14), 143001 (2008).
20. M. Meckel, D. Comtois, D. Zeidler, A. Staudte, D. Pavicic, H. C. Bandulet, H. Pepin, J. C. Kieffer, R. Drner, D. M. Villeneuve, and P. B. Corkum, "Laser-Induced Electron Tunneling and Diffraction," Science **320**(5882), 1478–1482 (2008).
21. C. I. Blaga, J. Xu, A. D. DiChiara, E. Sistrunk, K. Zhang, P. Agostini, T. A. Miller, L. F. DiMauro, and C. D. Lin, "Imaging ultrafast molecular dynamics with laser-induced electron diffraction," Nature **483**(7388), 194–197 (2012).

Optics EXPRESS

22. G. Sansone, E. Benedetti, F. Calegari, C. Vozzi, L. Avaldi, R. Flammini, L. Poletto, P. Villoresi, C. Altucci, R. Velotta, S. Stagira, S. D. Silvestri, and M. Nisoli, "Isolated Single-Cycle Attosecond Pulses," Science **314**(5798), 443–446 (2006).
23. E. Goulielmakis, M. Schultze, M. Hofstetter, V. S. Yakovlev, J. Gagnon, M. Uiberacker, A. L. Aquila, E. M. Gullikson, D. T. Attwood, R. Kienberger, F. Krausz, and U. Kleineberg, "Single-Cycle Nonlinear Optics," Science **320**(5883), 1614–1617 (2008).
24. T. Gaumnitz, A. Jain, Y. Pertot, M. Huppert, I. Jordan, F. Ardana-Lamas, and H. J. Worner, "Streaking of 43-attosecond soft-X-ray pulses generated by a passively CEP-stable mid-infrared driver," Opt. Express **25**(22), 27506 (2017).
25. J. Li, X. Ren, Y. Yin, K. Zhao, A. Chew, Y. Cheng, E. Cunningham, Y. Wang, S. Hu, Y. Wu, M. Chini, and Z. Chang, "53-attosecond X-ray pulses reach the carbon K-edge," Nat. Commun. **8**(1), 186 (2017).
26. J. Itatani, J. Levesque, D. Zeidler, H. Niikura, H. Ppin, J. C. Kieffer, P. B. Corkum, and D. M. Villeneuve, "Tomographic imaging of molecular orbitals," Nature **432**(7019), 867–871 (2004).
27. Y. Huismans, A. Rouze, A. Gijsbertsen, J. H. Jungmann, A. S. Smolkowska, P. S. W. M. Logman, F. Lpine, C. Cauchy, S. Zamith, T. Marchenko, J. M. Bakker, G. Berden, B. Redlich, A. F. G. van der Meer, H. G. Muller, W. Vermin, K. J. Schafer, M. Spanner, M. Y. Ivanov, O. Smirnova, D. Bauer, S. V. Popruzhenko, and M. J. J. Vrakking, "Time-Resolved Holography with Photoelectrons," Science **331**(6013), 61–64 (2011).
28. T. Marchenko, Y. Huismans, K. J. Schafer, and M. J. J. Vrakking, "Criteria for the observation of strong-field photoelectron holography," Phys. Rev. A **84**(5), 053427 (2011).
29. Y. Huismans, A. Gijsbertsen, A. S. Smolkowska, J. H. Jungmann, A. Rouzee, P. S. W. M. Logman, F. Lepine, C. Cauchy, S. Zamith, T. Marchenko, J. M. Bakker, G. Berden, B. Redlich, A. F. G. van der Meer, M. Y. Ivanov, T.-M. Yan, D. Bauer, O. Smirnova, and M. J. J. Vrakking, "Scaling Laws for Photoelectron Holography in the Midinfrared Wavelength Regime," Phys. Rev. Lett. **109**(1), 013002 (2012).
30. M. Meckel, A. Staudte, S. Patchkovskii, D. M. Villeneuve, P. B. Corkum, R. Drner, and M. Spanner, "Signatures of the continuum electron phase in molecular strong-field photoelectron holography," Nat. Phys. **10**(8), 594–600 (2014).
31. M. M. Liu, M. Li, C. Wu, Q. Gong, A. Staudte, and Y. Liu, "Phase Structure of Strong-Field Tunneling Wave Packets from Molecules," Phys. Rev. Lett. **116**(16), 163004 (2016).
32. L. Fechner, N. Camus, A. Krupp, J. Ullrich, T. Pfeifer, and R. Moshammer, "Creation and survival of autoionizing states in strong laser fields," Phys. Rev. A **92**(5), 051403 (2015).
33. S. G. Walt, N. Bhargava Ram, M. Atala, N. I. Shvetsov Shilovski, A. von Conta, D. Baykusheva, M. Lein, and H. J. Worner, "Dynamics of valence-shell electrons and nuclei probed by strong-field holography and rescattering," Nat. Commun. **8**(1), 15651 (2017).
34. H. Xie, M. Li, S. Luo, Y. Li, J. Tan, Y. Zhou, W. Cao, and P. Lu, "Photoelectron holography and forward scattering in atomic ionization by elliptically polarized laser pulses," Opt. Lett. **43**(14), 3220 (2018).
35. X.-B. Bian, Y. Huismans, O. Smirnova, K. J. Yuan, M. J. J. Vrakking, and A. D. Bandrauk, "Subcycle interference dynamics of time-resolved photoelectron holography with midinfrared laser pulses," Phys. Rev. A **84**(4), 043420 (2011).
36. M. He, Y. Li, Y. Zhou, M. Li, and P. Lu, "Temporal and spatial manipulation of the recolliding wave packet in strong-field photoelectron holography," Phys. Rev. A **93**(3), 033406 (2016).
37. Y. Li, Y. Zhou, M. He, M. Li, and P. Lu, "Identifying backward-rescattering photoelectron hologram with orthogonal two-color laser fields," Opt. Express **24**(21), 23697 (2016).
38. Y. Zhou, O. I. Tolstikhin, and T. Morishita, "Near-Forward Rescattering Photoelectron Holography in Strong-Field Ionization: Extraction of the Phase of the Scattering Amplitude," Phys. Rev. Lett. **116**(17), 173001 (2016).
39. M. He, Y. Li, Y. Zhou, M. Li, W. Cao, and P. Lu, "Direct Visualization of Valence Electron Motion Using Strong-Field Photoelectron Holography," Phys. Rev. Lett. **120**(13), 133204 (2018).
40. M. He, Y. Zhou, J. Tan, Y. Li, M. Li, and P. Lu, "Imaging charge migration in the asymmetric molecule with the holographic interference in strong-field tunneling ionization," J. Phys. B: At., Mol. Opt. Phys. **51**(24), 245602 (2018).
41. O. I. Tolstikhin and T. Morishita, "Adiabatic theory of ionization by intense laser pulses: Finite-range potentials," Phys. Rev. A **86**(4), 043417 (2012).
42. D. D. Hickstein, P. Ranitovic, S. Witte, X.-M. Tong, Y. Huismans, P. Arpin, X. Zhou, K. E. Keister, C. W. Hogle, B. Zhang, C. Ding, P. Johnsson, N. Toshima, M. J. J. Vrakking, M. M. Murnane, and H. C. Kapteyn, "Direct Visualization of Laser-Driven Electron Multiple Scattering and Tunneling Distance in Strong-Field Ionization," Phys. Rev. Lett. **109**(7), 073004 (2012).
43. J. Tan, Y. Zhou, M. He, Y. Chen, Q. Ke, J. Liang, X. Zhu, M. Li, and P. Lu, "Determination of the Ionization Time Using Attosecond Photoelectron Interferometry," Phys. Rev. Lett. **121**(25), 253203 (2018).
44. J. Tan, Y. Zhou, M. He, Q. Ke, J. Liang, Y. Li, M. Li, and P. Lu, "Time-resolving tunneling ionization via strong-field photoelectron holography," Phys. Rev. A **99**(3), 033402 (2019).
45. M. Li, H. Xie, W. Cao, S. Luo, J. Tan, Y. Feng, B. Du, W. Zhang, Y. Li, Q. Zhang, P. Lan, Y. Zhou, and P. Lu, "Photoelectron Holographic Interferometry to Probe the Longitudinal Momentum Offset at the Tunnel Exit," Phys. Rev. Lett. **122**(18), 183202 (2019).
46. G. Porat, G. Alon, S. Rozen, O. Pedatzur, M. Kruger, D. Azoury, A. Natan, G. Orenstein, B. D. Bruner, M. J. J. Vrakking, and N. Dudovich, "Attosecond time-resolved photoelectron holography," Nat. Commun. **9**(1), 2805 (2018).
47. W. Xie, M. Li, S. Luo, M. He, K. Liu, Q. Zhang, Y. Zhou, and P. Lu, "Nonadiabaticity-induced ionization time shift in strong-field tunneling ionization," Phys. Rev. A **100**(2), 023414 (2019).

Optics EXPRESS

48. S. Luo, M. Li, W. Xie, K. Liu, Y. Feng, B. Du, Y. Zhou, and P. Lu, "Exit momentum and instantaneous ionization rate of nonadiabatic tunneling ionization in elliptically polarized laser fields," Phys. Rev. A **99**(5), 053422 (2019).
49. D. B. Milosevic and W. Becker, "Attosecond pulse generation by bicircular fields: from pulse trains to a single pulse," J. Mod. Opt. **52**(2-3), 233–241 (2005).
50. E. Hasovic, A. Kramo, and D. B. Milosevic, "Energy- and angle-resolved photoelectron spectra of above-threshold ionization and detachment," Eur. Phys. J.: Spec. Top. **160**(1), 205–216 (2008).
51. D. B. Milosevic and W. Becker, "Improved strong-field approximation and quantum-orbit theory: Application to ionization by a bicircular laser field," Phys. Rev. A **93**(6), 063418 (2016).
52. E. Hasovic, W. Becker, and D. B. Milosevic, "Electron rescattering in a bicircular laser field," Opt. Express **24**(6), 6413 (2016).
53. N. I. Shvetsov-Shilovski and M. Lein, "Effects of the Coulomb potential in interference patterns of strong-field holography with photoelectrons," Phys. Rev. A **97**(1), 013411 (2018).
54. A. Kramo, E. Hasović, D. B. Milošević, and W. Becker, "Above-threshold detachment by a two-color bicircular laser field," Laser Phys. Lett. **4**(4), 279–286 (2007).
55. H. Van-Hung and L. Van-Hoang, "Retrieval of target structure information from laser-induced photoelectrons by few-cycle bicircular laser fields," Phys. Rev. A **95**(3), 031402 (2017).
56. A. Gazibegović-Busuladžić, W. Becker, and D. B. Milošević, "Helicity asymmetry in strong-field ionization of atoms by a bicircular laser field," Opt. Express **26**(10), 12684 (2018).
57. J. Ngoko Djiokap, S. Hu, L. Madsen, N. Manakov, A. Meremianin, and A. F. Starace, "Electron Vortices in Photoionization by Circularly Polarized Attosecond Pulses," Phys. Rev. Lett. **115**(11), 113004 (2015).
58. C. A. Mancuso, D. D. Hickstein, P. Grychtol, R. Knut, O. Kfir, X.-M. Tong, F. Dollar, D. Zusin, M. Gopalakrishnan, C. Gentry, E. Turgut, J. L. Ellis, M.-C. Chen, A. Fleischer, O. Cohen, H. C. Kapteyn, and M. M. Murnane, "Strong-field ionization with two-color circularly polarized laser fields," Phys. Rev. A **91**(3), 031402 (2015).
59. C. A. Mancuso, D. D. Hickstein, K. M. Dorney, J. L. Ellis, E. Hasovic, R. Knut, P. Grychtol, C. Gentry, M. Gopalakrishnan, D. Zusin, F. J. Dollar, X.-M. Tong, D. B. Milosevic, W. Becker, H. C. Kapteyn, and M. M. Murnane, "Controlling electron-ion rescattering in two-color circularly polarized femtosecond laser fields," Phys. Rev. A **93**(5), 053406 (2016).
60. C. A. Mancuso, K. M. Dorney, D. D. Hickstein, J. L. Chaloupka, X. M. Tong, J. L. Ellis, H. C. Kapteyn, and M. M. Murnane, "Observation of ionization enhancement in two-color circularly polarized laser fields," Phys. Rev. A **96**(2), 023402 (2017).
61. S. Eckart, M. Kunitski, I. Ivanov, M. Richter, K. Fehre, A. Hartung, J. Rist, K. Henrichs, D. Trabert, N. Schlott, L. P. H. Schmidt, T. Jahnke, M. S. Schffler, A. Kheifets, and R. Dorner, "Subcycle interference upon tunnel ionization by counter-rotating two-color fields," Phys. Rev. A **97**(4), 041402 (2018).
62. S. Eckart, K. Fehre, N. Eicke, A. Hartung, J. Rist, D. Trabert, N. Strenger, A. Pier, L. Schmidt, T. Jahnke, M. Schoffler, M. Lein, M. Kunitski, and R. Dorner, "Direct Experimental Access to the Nonadiabatic Initial Momentum Offset upon Tunnel Ionization," Phys. Rev. Lett. **121**(16), 163202 (2018).
63. M. Li, W.-C. Jiang, H. Xie, S. Luo, Y. Zhou, and P. Lu, "Strong-field photoelectron holography of atoms by bicircular two-color laser pulses," Phys. Rev. A **97**(2), 023415 (2018).
64. K.-J. Yuan and A. D. Bandrauk, "Above-threshold ionization in molecules by intense multiple-frequency circularly polarized laser pulses," Phys. Rev. A **98**(2), 023413 (2018).
65. M. Abu-samha and L. B. Madsen, "Probing atomic and molecular targets by intense bicircular counter-rotating laser fields," J. Phys. B: At., Mol. Opt. Phys. **51**(13), 135401 (2018).
66. M. Han, P. Ge, Y. Shao, Q. Gong, and Y. Liu, "Attoclock Photoelectron Interferometry with Two-Color Corotating Circular Fields to Probe the Phase and the Amplitude of Emitting Wave Packets," Phys. Rev. Lett. **120**(7), 073202 (2018).
67. P. Ge, M. Han, Y. Deng, Q. Gong, and Y. Liu, "Universal Description of the Attoclock with Two-Color Corotating Circular Fields," Phys. Rev. Lett. **122**(1), 013201 (2019).
68. N. Eicke and M. Lein, "Attoclock with counter-rotating bicircular laser fields," Phys. Rev. A **99**(3), 031402 (2019).
69. L. Medisauskas, J. Wragg, H. van der Hart, and M. Y. Ivanov, "Generating Isolated Elliptically Polarized Attosecond Pulses Using Bichromatic Counterrotating Circularly Polarized Laser Fields," Phys. Rev. Lett. **115**(15), 153001 (2015).
70. D. M. Reich and L. B. Madsen, "Illuminating Molecular Symmetries with Bicircular High-Order-Harmonic Generation," Phys. Rev. Lett. **117**(13), 133902 (2016).
71. K. M. Dorney, J. L. Ellis, C. Hernandez-Garcia, D. D. Hickstein, C. A. Mancuso, N. Brooks, T. Fan, G. Fan, D. Zusin, C. Gentry, P. Grychtol, H. C. Kapteyn, and M. M. Murnane, "Helicity-Selective Enhancement and Polarization Control of Attosecond High Harmonic Waveforms Driven by Bichromatic Circularly Polarized Laser Fields," Phys. Rev. Lett. **119**(6), 063201 (2017).
72. L. Barreau, K. Veyrinas, V. Gruson, S. J. Weber, T. Auguste, J.-F. Hergott, F. Lepetit, B. Carre, J.-C. Houver, D. Dowek, and P. Salieres, "Evidence of depolarization and ellipticity of high harmonics driven by ultrashort bichromatic circularly polarized fields," Nat. Commun. **9**(1), 4727 (2018).
73. M. D. Feit, J. A. Fleck, and A. Steiger, "Solution of the Schrödinger equation by a spectral method," J. Comput. Phys. **47**(3), 412–433 (1982).

Optics EXPRESS

74. S. Chelkowski, C. Foisy, and A. D. Bandrauk, "Electron-nuclear dynamics of multiphoton H_2^+ dissociative ionization in intense laser fields," Phys. Rev. A **57**(2), 1176–1185 (1998).
75. X. M. Tong, K. Hino, and N. Toshima, "Phase-dependent atomic ionization in few-cycle intense laser fields," Phys. Rev. A **74**(3), 031405 (2006).
76. X. M. Tong, S. Watahiki, K. Hino, and N. Toshima, "Numerical Observation of the Rescattering Wave Packet in Laser-Atom Interactions," Phys. Rev. Lett. **99**(9), 093001 (2007).
77. M. Protopapas, C. H. Keitel, and P. L. Knight, "Atomic physics with super-high intensity lasers," Rep. Prog. Phys. **60**(4), 389–486 (1997).
78. L. Lehtovaara, J. Toivanen, and J. Eloranta, "Solution of time-independent Schrödinger equation by the imaginary time propagation method," J. Comput. Phys. **221**(1), 148–157 (2007).